

Electrochemical Impedance Measurements in Scanning Ion Conductance Microscopy

Viacheslav Shkirskiy,* Minkyung Kang, Ian J. McPherson, Cameron L. Bentley, Oluwasegun J. Wahab, Enrico Daviddi, Alex W. Colburn, and Patrick R. Unwin*

Cite This: *Anal. Chem.* 2020, 92, 12509–12517

Read Online

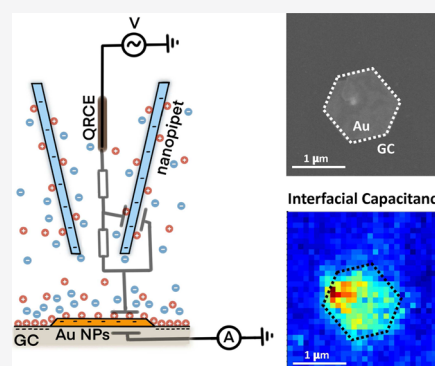
ACCESS |

Metrics & More

Article Recommendations

Supporting Information

ABSTRACT: Electrochemical impedance spectroscopy (EIS) is a versatile tool for electrochemistry, particularly when applied locally to reveal the properties and dynamics of heterogeneous interfaces. A new method to generate local electrochemical impedance spectra is outlined, by applying a harmonic bias between a quasi-reference counter electrode (QRCE) placed in a nanopipet tip of a scanning ion conductance microscope (SICM) and a conductive (working electrode) substrate (two-electrode setup). The AC frequency can be tuned so that the magnitude of the impedance is sensitive to the tip-to-substrate distance, whereas the phase angle is broadly defined by the local capacitive response of the electrical double layer (EDL) of the working electrode. This development enables the surface topography and the local capacitance to be sensed reliably, and separately, in a single measurement. Further, self-referencing the probe impedance near the surface to that in the bulk solution allows the local capacitive response of the working electrode substrate in the overall AC signal to be determined, establishing a quantitative footing for the methodology. The spatial resolution of AC-SICM is an order of magnitude larger than the tip size (100 nm radius), for the studies herein, due to frequency dispersion. Comprehensive finite element method (FEM) modeling is undertaken to optimize the experimental conditions and minimize the experimental artifacts originating from the frequency dispersion phenomenon, and provides an avenue to explore the means by which the spatial resolution could be further improved.



1. INTRODUCTION

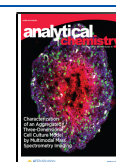
Electrochemical impedance spectroscopy (EIS) has become an important tool in a wide range of applications, including label-free detection for biosensors and drug screening,¹ measurement of charge-transfer kinetics and the corrosion of metals,^{2,3} assessing passive layers with thicknesses down to the nanometer level,⁴ analysis of the state of charge in batteries,⁵ and determining the electronic structure of semiconductors in photovoltaics.⁶ Despite its unique capabilities, EIS is first and foremost a macroscopic technique applied to an entire electrode surface.

An early attempt to implement more localized EIS in a scanning regime was done in a conventional three-electrode setup with the placement of the reference electrode (RE) and the counter electrode in a capillary, with an 80 μm orifice, that was used to map the surface of a 304 stainless steel working electrode (WE) under complete immersion in 1 M Na₂SO₄.⁷ The complex distribution of the electric field under these conditions did not allow quantitative analysis at that time. To simplify data interpretation, this approach was translated to the electrochemical droplet cell (EDC) configuration, where the active area is limited to a small region of the surface of interest under a droplet formed at the end of a fluidic probe.^{8–10} In this setup, EIS has been successfully applied with a spatial

resolution ranging from tens to hundreds of micrometers to map defects in coatings and assess ultrathin Al films⁹ and passivation of polycrystalline Hf metal^{8,10} and Hf–Ta, Nb–Ti, and Hf–Ti metal libraries.¹¹

A similar resolution has been achieved using scanning electrochemical microscopy operated in the alternative current (AC) mode (AC-SECM).^{12,13} Demonstrated on iron oxide surfaces¹⁴ and low-carbon steel coated with tin and a layer of epoxyphenolic varnish,¹⁵ AC-SECM provided local information on double-layer capacitance and interfacial charge-transfer resistance. However, the AC response was convoluted by the tip-to-substrate distance, requiring complementary information on the surface topography.¹⁶ This limitation was removed in local EIS measurements using atomic force microscopy (AFM) with a conductive tip as the counter electrode in a two-electrode mode.^{17–19} Examples of local EIS-AFM measurements include characterization of the conductive channels of a

Received: June 2, 2020
Accepted: August 4, 2020
Published: August 4, 2020



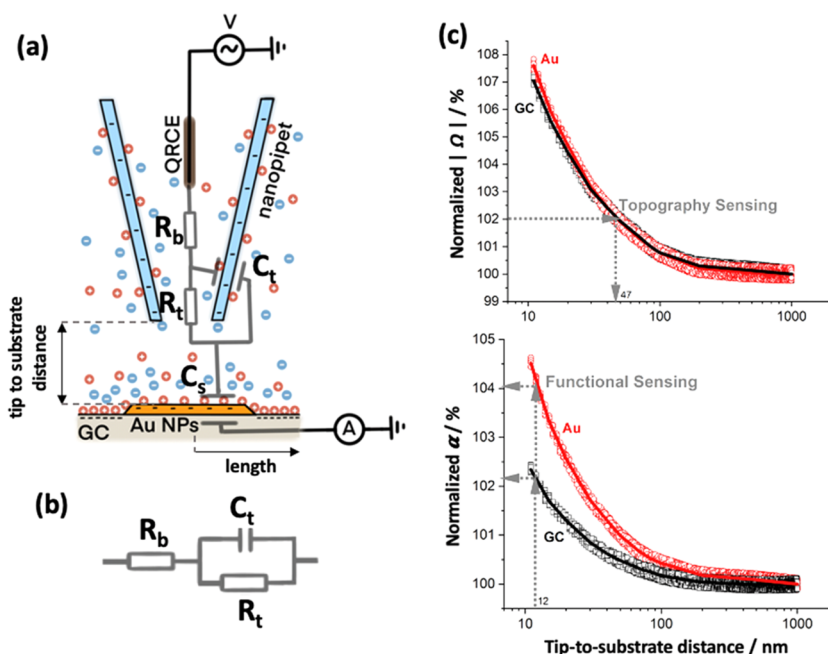


Figure 1. (a) AC-SICM configuration, with a QRCE in the nanopipet channeling AC current through the substrate, of a Au nanoplate (AuNP) on a surface of glassy carbon (GC) as an example. The equivalent circuit illustrates the current pathway and elements contributing to the impedance response. (b) Simplified equivalent circuit used to fit the impedance spectra at a 1 μm distance of the nanopipet tip from the substrate, where the capacitance from the substrate, C_s , has a minor contribution to the overall impedance response. (c) Approach curves of normalized magnitudes of impedance and phase angle for a polycrystalline Au and GC macroelectrode substrates, biased at 0 V with respect to Ag/AgCl QRCE in the tip (100 nm radius), in 50 mM KCl. The dots show 10 overlaid sequential experimental approach curves. The solid lines are numerically generated curves in COMSOL Multiphysics (see the text for details).

Nafion membrane surface,²⁰ intergranular corrosion of AISI 304 stainless steel,²¹ and oxygen reduction reaction kinetics at platinum/Nafion contacts.²² The use of a small counter electrode (i.e., AFM tip), however, complicates the quantitative analysis of impedance spectra because the electric field distribution depends strongly on the frequency of the applied harmonic bias.^{23,24}

Rigorous theoretical analysis of impedance spectra utilized a five-electrode configuration, where local electrochemical impedance spectra (LEIS) were generated by measuring the local AC current density over a WE as part of a conventional three-electrode configuration,^{24,25} with an additional two-electrode probe. The influence of cell and electrode geometries,^{26–30} probe position,³¹ and probe geometry^{32,33} on the LEIS was clarified, allowing the direct comparison of local and global impedances. This technique was used to identify active areas and quantify the kinetics of local metal dissolution,³⁴ pitting,³⁵ and the degradation of polymer-modified surfaces of Zn,^{36,37} Al2024,³⁸ and carbon steel.^{39,40} The spatial resolution of LEIS is typically restricted to the microscale owing to difficulties of scaling down the probe size, as well as controlling the tip-to-substrate distance during scanning.^{36,41}

Recent years have seen significant advances in scanning ion conductance microscopy (SICM), scanning electrochemical cell microscopy (SECCM), and hybrids of these techniques that use pipet-based probes to achieve tens of nanometer spatial resolution, with excellent temporal resolution.^{42–47} Usually, in SICM, a DC bias is applied between a quasi-reference counter (QRCE) in the nanopipet probe, filled with the electrolyte, and one in the bulk solution to generate an ion current that allows topographical, surface charge, and surface activity mapping.^{46,48} Bias modulation (BM) in this configuration has also been used as a means of generating an

alternating component of the ion current that can be used as a feedback signal for SICM positioning and to provide functional information.^{49–52}

In the present work, we use a two-electrode configuration, wherein the QRCE placed in the tip is biased with respect to a grounded conductive (electrode) substrate, so as to channel the AC bias through the electrical double layer (EDL) (Figure 1a). We show that this simplified two-electrode setup is attractive for generating local EIS: the magnitude of impedance can be used for precise probe positioning (i.e., topographical sensing), while phase angle values can be utilized to quantify the properties of the EDL. Furthermore, we demonstrate that self-referencing of the tip impedance spectrum recorded near the substrate surface to that recorded with the tip in the bulk allows isolation of the local impedance of the substrate. We used AC-SICM to synchronously map the topography and local capacitance of Au nanoplates (AuNPs) drop-cast onto a glassy carbon (GC) electrode, which simulates the complex catalyst-on-support configuration of practical electrodes used for sensing and energy applications (e.g., for electrocatalysis). Underpinned by complementary numerical analysis using finite element method (FEM) modeling, this work highlights the future prospects of this new mode of SICM for the functional characterization of electrochemical interfaces.

2. EXPERIMENTAL SECTION

2.1. Materials. All experiments were performed in 50 mM KCl (Sigma-Aldrich) solutions in Milli-Q reagent-grade water (resistivity of ca. 18.2 M Ω cm at 25 $^{\circ}\text{C}$). Au foils (Goodfellow, U.K., 99.999%) of 25 \times 25 \times 0.1 mm were sectioned using an abrasive cutter to give a sample of ca. 5 \times 5 mm size, which was mounted in a carbon-based conductive mount using a

Buehler SimpliMet 3000 Mounting Press (Buehler). A glassy carbon (GC) plate of $10 \times 10 \times 2$ mm (HTW-Germany) was used as received. Both GC and Au macroelectrodes were mirror-polished with a $0.05 \mu\text{m}$ Al_2O_3 (Buehler) slurry to ensure their surfaces were flat and clean. They were subsequently washed by ultrasonification in deionized water and dried under a stream of nitrogen prior to use. The AuNPs were prepared by reducing AuCl_4^- (from HAuCl_4) with lemongrass extract, as per a literature procedure.⁵³ The AuNPs were drop-cast from the resuspended solution onto GC. These single-crystalline (111)-oriented AuNPs are mainly triangular- or hexagonal-shaped, with thickness ca. 10–15 nm and range in size from ca. 100 nm to $>1 \mu\text{m}$, as shown in the Supporting Information (SI), Figure S1.

Ag/AgCl QRCEs were prepared by anodizing a 0.125 mm diameter annealed silver wire (Goodfellow, U.K., 99.99%) at +1 V vs Pt counter electrode in a saturated KCl solution for 5–10 min. QRCEs of this type possess long-term stability and do not contaminate the surface investigated in a variety of electrolyte solutions on the time scale of SICM and related measurements.⁵⁴

2.2. AC-SICM Instrumentation. The instrumentation was modified from that described in detail elsewhere.^{50,51,55} Briefly, single-barreled nanopipet probes were pulled with a Sutter P2000 pipet puller from a borosilicate glass capillary of 1.2 OD \times 0.69 ID \times 100 L mm (30-0044 GC120F-10 Harvard Apparatus) to produce a circular tapered end of internal radius 100 nm. Each nanopipet was thoroughly characterized by transmission electron microscopy (TEM) to define the precise geometry of the tip orifice used as an input for numerical simulations (vide infra).⁵⁶ The tip geometry was typical of that used in a number of recent SICM studies.^{48,51,55,57} Each nanopipet was filled with 50 mM KCl together with a Ag/AgCl wire placed in the back to serve as a QRCE. All potentials are quoted with respect to Ag/AgCl in 50 mM KCl having a 60 mV potential difference vs Ag/AgCl in 3 M KCl, measured experimentally, and, as expected, based on the dependence of the chloride ion activity coefficient on the KCl concentration.⁵⁸ This difference was consistent across all tested Ag/AgCl QRCEs, and the measured potential was stable on the time scale of AC-SICM experiments.⁵⁴ The top (back) of nanopipets was sealed with superglue (Loctite) to minimize electrolyte evaporation from the back.

The SICM probe was mounted on a *z*-piezoelectric positioner (P-753.3CD with an E-665 controller, Physik Instrumente (PI), Germany), while the sample was placed on an *xy*-piezoelectric stage (P-621.2CD with an E-625 controller, PI, Germany). The *z*-stage was also equipped with a stepper motor (8303 Picomotor Actuator, Newport) for coarse movement. A lock-in amplifier (SR830, Stanford Research Systems) was used to generate an oscillating bias of 320 Hz with a 50 mV peak-to-peak (ptp) amplitude and to detect the AC component of the oscillating ion current between the QRCE in the nanopipet and the sample (Figure 1a). A custom wideband current-to-voltage converter (100 kHz, 3dB) was used to measure the current at the WE substrate. All experiments were done at 0.0 V DC bias, where there were no significant faradaic reactions at the conductive interfaces studied, so as to focus on EDL properties, as confirmed by the absence of significant DC ion current between the tip QRCE and the substrate electrode.^{48,51,57,59}

For the approach measurements, the nanopipet was moved toward the surface at a speed of $4 \mu\text{m s}^{-1}$ until the surface was

detected as a 2% change of impedance modulus defined as the set point. AC-SICM maps were generated in a hopping mode, where a series of nanopipet approaches were made in a predefined grid pattern over AuNPs drop-cast on GC. At each point, the nanopipet approached the surface at a speed of $4 \mu\text{m s}^{-1}$ until the impedance modulus changed by 2% relative to the value at that pixel with the nanopipet in the bulk ($1 \mu\text{m}$ from the surface). After this point, the probe was set to retract by a distance of $1 \mu\text{m}$ with a velocity of $20 \mu\text{m s}^{-1}$. This procedure resulted in an additional 35 nm approach (equivalent to 7% set point) toward the substrate relative to the 2% set point, as described previously,⁶⁰ which could be measured accurately from the impedance modulus approach curve at each pixel (Figure 1 and SI, Figure S2). Topographical maps were generated from the *z*-position at the 2% set point, while capacitance maps were obtained from phase angle values at the closest position of the probe to the substrate with 35 nm overshoot (vide infra). Secondary electron scanning electron microscopy (SEM) images of the samples were acquired with a Zeiss SIGMA FE-SEM (Zeiss, Germany), at 5 kV using InLens mode. The surface of the GC substrate was scratched with a scalpel blade to form a square grid of ca. $500 \mu\text{m}$ for a coarse location of AuNP during AC-SICM. Additionally, we used the nanopipet tip to scratch the surface of the GC near AuNPs after AC-SICM scans so as to facilitate the precise location of nanoplates in postmortem SEM analysis.

The SICM setup was situated in an aluminum Faraday cage equipped with heat sinks and vacuum panels to minimize the noise and thermal drift. The Faraday cage was positioned on an optical table (RS2000, Newport) with automatic leveling isolators (Newport, S-2000A-423.5).

Data acquisition and instrumentation control utilized an FPGA card (PCIe-7852R) controlled by a LabVIEW 2016 (National Instruments) interface running the Warwick Electrochemical Scanning Probe Microscopy (WEC-SPM, www.warwick.ac.uk/electrochemistry) software. Current signals were measured every 2 μs , averaged every 64 points, with one further point for transfer, to give a data acquisition rate of 130 μs per point.

After experiments, the raw data were processed using the Matlab R2018a software package. Data plotting was carried out using the Matlab R2018a and OriginPro 2019 64bit software packages. All maps were plotted in Matlab, with no data interpolation.

2.3. SICM Impedance Spectra Measurements. Impedance spectra in the SICM (two-electrode) format were measured using a Gamry Femtostat (FAS2-38039), with spectra acquired using Gamry Framework Data Acquisition Software (6.04). The AC-SICM approach described above was used to position the nanopipet close to the surface (7% threshold in the impedance modulus), whereupon the electrochemical circuit was switched to the Femtostat and the nanopipet was held stationary for 75 s while a complete impedance spectrum was recorded. The nanopipet was then retracted by a distance of $1 \mu\text{m}$, and a second “bulk” EIS spectrum was recorded. Subsequent approaches of the nanopipet back to the surface showed that thermal drift changed the probe-to-distance position by no more than 5 nm over the time of spectrum acquisition (SI, Figure S3). Equivalent circuit models were fitted using a simplex method with 300 iterations using Gamry Echem Analyst software. The goodness of fit and Kramers–Kronig validation gave less than 0.5% error for all reported data.

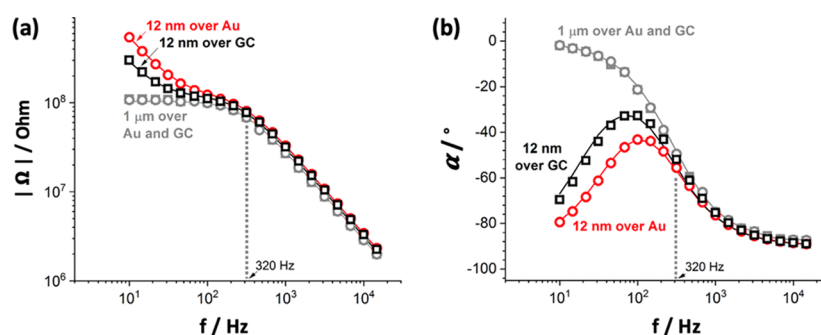


Figure 2. Bode plot of AC-SICM impedance measurements (100 nm radius tip in 50 mM KCl) at 1 μm and 12 nm tip-to-substrate distances over polycrystalline Au (red) and GC (black) macroelectrodes: (a) modulus of impedance and (b) phase angle as a function of frequency. Spectra in the bulk over both Au and GC closely overlay. Points indicate experimental data and solid lines show fitting curves using the equivalent circuits in Figure 1a (at 12 nm) and 1b (at 1 μm). The parameters used for fitting are presented in Table 1.

2.4. FEM Simulations. We adapted the numerical model previously developed for BM-SICM.^{48,50,51} Briefly, a two-dimensional (2D) axisymmetric FEM simulation was performed in COMSOL Multiphysics (5.4) using the transport of diluted species and electrostatics modules for a 100 nm radius borosilicate nanopipet (geometrical arrangement of the probe determined from TEM; SI, Figure S4) in 50 mM KCl solution. The surface charge density on the nanopipet tip was -15 mC m^{-2} , within the range of the previously reported simulations.^{51,59,61,62} We employed the Gouy–Chapman–Stern model for the EDL of the working electrode substrate. The compact double layer (CDL) of the substrate was taken into account through a potential drop formulated as a surface charge condition (eqs 1 and 2). Harmonic bias perturbation boundary conditions were used to simulate the AC behavior of the AC-SICM setup. Further details of the FEM model are given in SI-7.

3. RESULTS AND DISCUSSION

3.1. Approach Curves. As noted in the Experimental Section, nanopipets (100 nm in radius) were made to approach the surface at a velocity of $4 \mu\text{m s}^{-1}$ in 50 mM KCl to both GC and Au macroelectrodes. An AC bias of 50 mV ptp amplitude and 320 Hz frequency (for fast data acquisition) was applied at a DC bias of 0 V vs Ag/AgCl at the substrate surface (applied versus the QRCE in the probe tip). Absolute values of the phase angle and magnitude of the impedance were recorded during the approach and normalized with respect to the response of the tip in the bulk, as reported for BM-SICM.^{51,55} The approaches were reproduced 10 times sequentially, with typical curves presented in Figure 1c.

The approach curves are similar to the previously reported data for BM-SICM (with the second electrode in the bulk solution):⁴⁹ both impedance magnitude and phase angle are stable far away from the surface with a steep change when the nanopipet is within approximately a tip radius of the substrate. Remarkably, normalized impedance values show identical behavior over both GC and Au interfaces, while normalized phase angle values depend on the type of the substrate. An increase in the magnitude of the impedance as the nanopipet approaches the substrate is due to an increase in the system resistance due to some blocking of the ion current path in the narrow gap. Importantly, these data show that AC-SICM enables the surface topography and the surface properties to be sensed in a single approach, using the impedance magnitude for topographical feedback (setting the tip–substrate distance)

and the magnitude of the phase angle for functional sensing. The normalized values of impedance and phase angle in the experimental approach curves in Figure 1c were overlaid with simulation predictions, as reported below.

3.2. Impedance Measurements. To explore the differences in the phase angle behavior over the GC and Au macroelectrodes, we performed impedance measurements with a nanopipet (100 nm radius) at 1 μm and 12 nm tip-to-substrate distances from the two macroelectrode surfaces in 50 mM KCl. We expect no faradaic reactions on either substrate (i.e., within the double-layer potential region) under these conditions.⁴² We approached the probe with a 7% feedback of impedance magnitude and held it stationary for 75 s while an impedance spectrum was recorded (10 kHz to 10 Hz, 6 points per decade). Then, the probe was retracted by 1 μm distance from the surface and the impedance spectrum was recorded again. Subsequent approaches showed that the rate of thermal drift was ca. 0.08 nm s^{-1} (SI, Figure S3), consistent with previous SICM measurements,^{55,63} and so based on the data acquisition time, the extent of thermal drift at high frequencies ($>100 \text{ Hz}$) should be minimal ($<1 \text{ nm}$), which is within the noise level of the piezo-positioning system used.⁶⁴ In principle, there could be ca. 5 nm displacement of the probe during a whole impedance scan, which could cause a relatively small error in the estimation of impedance and phase angle as illustrated in the approach curves in Figure 1c.

Impedance measurements over both GC and Au are shown in Bode coordinates in Figure 2 (Nyquist plot, Figure S5). The impedance spectra at a 1 μm distance are nearly identical over both substrates because the impedance of the tip dominates the AC response, with the shape of the impedance modulus and phase angle curves consistent with previous measurements on nanopipets.^{55,65} At high frequencies of 10–1 kHz, the capacitive response of the tip walls dominates the overall signal (phase angle of ca. -90°), resulting in a linear correlation between the impedance magnitude and frequency in the Bode plot. At low frequencies of 100–10 Hz, the resistance of the tip end governs the AC signal, giving a phase angle of ca. 0° and a constant value of impedance of ca. $100 \text{ M}\Omega$. Between these limiting cases, the response at intermediate frequencies is governed by both tip resistance and tip capacitance. We used the Randles equivalent circuit in Figure 1b to fit the experimental data (Table 1). Absolute values of the resistance ($R_t = 102 \text{ M}\Omega$) and capacitance of the tip orifice ($C_t = 5.5 \text{ pF}$) are consistent with the previously reported data for a ca. 100 nm radius tip in 50 mM KCl.^{55,56}

Table 1. Parameters Used to Fit the Impedance Data in Figure 2, Using the Equivalent Circuits in Figure 1a (at 12 nm) and 1b (at 1 μm)^a

distance		R_b/Ω	$R_t/\text{M}\Omega$	C_t/pF	C_s/pF
1 μm	Au	200	102	5.5	
	GC	200	102	5.5	
12 nm	Au	200*	110	5.5*	29
	GC	200*	109	5.5*	61

^aThe goodness of fit and Kramers–Kronig validation gave less than 0.5% error. The asterisk indicates fixed parameters during the fitting.

At frequencies of >1 kHz, the impedance data at a 12 nm tip-to-substrate distance appear to be similar to the data at 1 μm distance, as expected given the major contribution of the tip to the overall impedance response at high frequencies. At intermediate frequencies of 100 Hz to 1 kHz, impedance values over GC and Au at 12 nm are essentially identical, whereas the phase angle shows a subtle difference with values over Au being slightly lower than for GC. The observation of the phase angle being more sensitive to the properties of the biased substrate is expected, given the approach curves at 320 Hz reported in Figure 1c.

At low frequencies of <100 Hz, the spectra are broadly different at 12 nm and 1 μm tip-to-substrate distances, apparent from the abrupt increase of impedance magnitude and the sudden change of phase angle, with decreasing frequency, which is more pronounced over the Au substrate. We included the capacitance of the EDL (C_s) in series to a Randles circuit (Figure 1a) to fit the impedance spectra at a 12 nm tip-to-substrate distance (Table 1). The bulk properties of the tip were fixed (R_b and C_t) from the impedance measurements at 1 μm , leaving R_t and C_s to be fitted, with the values shown in Table 1. In this model, R_t is determined by the access resistance between the pipet tip and the sample surface (end of the tip and the gap). It increases from 102 to ca. 110 M Ω by approaching both GC and Au substrates and does not depend on the type of the substrate, as would be the case for conventional SICM, without substrate surface charge effects.⁴⁸

The capacitance of the EDL manifests on the impedance spectra at low frequencies <100 Hz. The extracted values of C_s were 29 and 61 pF for Au and GC, respectively (Table 1). For comparison, macroscopic impedance measurements indicated a capacitance of 20 $\mu\text{F cm}^{-2}$ for Au and 40 $\mu\text{F cm}^{-2}$ for GC macroelectrodes at the same DC bias of 0 V vs Ag/AgCl in 50 mM KCl (SI, Figure S6), using the geometric surface area for normalization. Matching the C_s values derived from SICM with the macroscopic measurements requires a probed area of ca. 150 μm^2 , corresponding to a disk of ca. 7 μm radius, compared to the tip radius of 100 nm. This discrepancy can originate from the displacement of the probe due to thermal drift at low frequencies or/and from the frequency dispersion of the electric field, as reported for local EIS-AFM measurements in the case of small counter electrodes^{23,24} (vide infra).

3.3. Numerical Simulations of Electric Field Distribution. We simulated the harmonic perturbation of the EDL and estimated the distribution of the electric field near the tip orifice for the two-electrode AC-SICM measurements. Briefly, ions are considered as point charges, and ionic transport is assumed to follow the Nernst–Planck–Poisson relation.^{48,50,51} The tip geometry was defined from complementary TEM analysis (SI, Figure S4).

The model details are provided in SI-7. As an extension of our previously reported model,^{48,50,51} the potential drop at the substrate (working) electrode was formulated as a surface charge (σ_s) condition at a conductive interface⁶⁶

$$\sigma_s = C_s \times \Delta\phi \quad (1)$$

$$\Delta\phi = \phi_M - \phi \quad (2)$$

where ϕ_M is the overpotential of the EDL with respect to the potential of zero charge (PZC), and ϕ is the potential at the outer Helmholtz plane. The PZC of GC and Au was estimated as −0.25 and 0 V vs Ag/AgCl in 50 mM KCl (see SI, Figure S6). Application of eq 1 suggests a linear relationship between σ_s and $\Delta\phi$ that was seen experimentally in a potential range of ± 0.2 V vs PZC for both substrates (SI, Figure S6).

The approach curves obtained from numerical simulations are overlaid with the experimental data in Figures 1c and S2, justifying the numerical model as a robust framework for rationalizing experimental AC-SICM data in parallel with the equivalent circuit analysis described above. Furthermore, the model was used to explore the spatial distribution of the electric field in AC-SICM. Figure 3a depicts the spatial

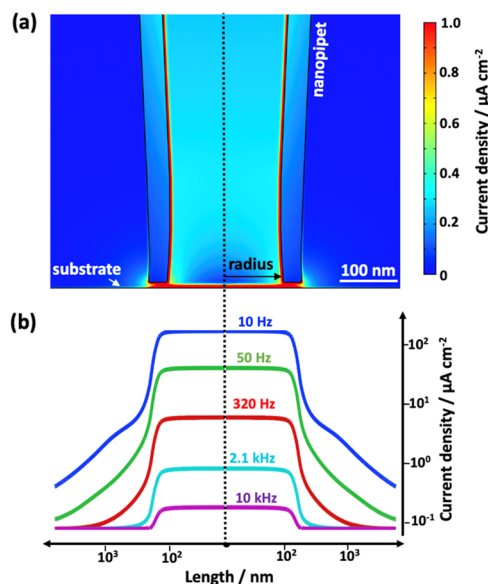


Figure 3. Distribution of the current density modulus over a substrate of 20 $\mu\text{F cm}^{-2}$ at 0 V vs PZC and 50 mV ptp amplitude from numerical simulations for a 100 nm radius nanopipet tip in 50 mM KCl at a 12 nm tip-to-substrate distance. (a) Two-dimensional (2D) representation of the current density distribution at 320 Hz. (b) Current density distribution on the surface of the substrate as a function of the radial distance (length) from the location of the center of the tip at different frequencies. The dotted line represents the symmetry axis.

distribution of the current density for the 100 nm radius tip with a 12 nm tip-to-substrate distance relative to a biased interface of $C_s = 20 \mu\text{F cm}^{-2}$ at a frequency of 320 Hz and 50 mV ptp amplitude. The current generated drops predominantly on the walls of the tip, in the tip orifice, and on the working electrode substrate in the region of the tip, in agreement with the equivalent circuit in Figure 1a.

We plotted the precise values of current density along the substrate for several harmonic frequency values (Figure 3b; note the log current density scale). The magnitude of current

density is constant within the tip footprint and then decays significantly with radial distance beyond the nanopipet tip area to negligible values, in a similar manner to the two-electrode AC-SICM configuration.⁶⁷ The extent of the decay depends on the frequency of harmonic perturbation. At high frequencies of >ca. 2.1 kHz, the current density decreases dramatically immediately beyond the tip and only the area beneath the tip is probed. At lower frequencies of <ca. 320 Hz, the current density spreads over a wider area and decreases the spatial resolution.

The frequency dependence of the current distribution (often called frequency dispersion)^{68,69} has been observed for local EIS-AFM with a conductive counter electrode tip.^{23,24} This effect also applies to this AC-SICM configuration, where the harmonic bias is channeled through the nanosized nanopipet tip. The impedance of a 100 nm radius disk of the substrate (equivalent to the minimum tip radius footprint) with a capacitance $20 \mu\text{F cm}^{-2}$ is $80 \text{ G}\Omega$ at 320 Hz and decreases at higher frequencies. It is ca. 800 times larger than the experimentally measured tip resistance of $110 \text{ M}\Omega$ at the 12 nm tip-to-substrate distance (Table 1). The current follows the least resistive path according to Laplace's law. This massive difference of the tip and local substrate impedances results in a smearing of current lines on the substrate to distances larger than the tip size.

Significant frequency dispersion can be detrimental for the quantification of the local properties of conductive interfaces.²³ For impedance imaging, we thus used a single frequency (320 Hz), which was sufficiently low to be sensitive to the interfacial capacitance but high enough to speed up the analysis at each pixel to avoid thermal drift issues (SI, Figure S3). A self-referencing hopping mode was implemented, where a bulk measurement (at $1 \mu\text{m}$ from the substrate) enabled the elucidation of R_b and C_t parameters (refer to Figure 1a) at every hop (i.e., pixel in map). Further, as also discussed above, R_t depends on the tip-to-substrate distance and is constant for approaches over Au and GC (Table 1). Thus, in a single approach, the magnitude of the phase angle at this frequency could be used to quantify the local capacitance. We examined the spatial resolution and quantitative aspects of AC-SICM experimentally through imaging the local capacitive properties of AuNP drop-cast on GC.

3.4. Simultaneous Topography and Capacitance Imaging. Scans were performed over AuNPs drop-cast on GC in a hopping mode to examine the spatial resolution and quantitative aspects of AC-SICM experimentally (Figure 4). At each hop (pixel), the nanopipet (100 nm in radius) was approached at $4 \mu\text{m s}^{-1}$ using 2% relative feedback values of impedance magnitude (corresponds to a 47 nm probe-to-substrate distance—Figure 1c) for the probe position and topography scan. As discussed, the probe overshoot 35 nm closer to the surface before the probe retraction (see SI, Figure S2) and the phase angle values were taken at this closer position (higher sensitivity) and further analyzed to obtain information about the properties of the EDL. The lateral movement and the retraction speed of the probe were $20 \mu\text{m s}^{-1}$. With these parameters, it was possible to perform synchronous topography and impedance imaging with an acquisition rate of ca. 8 pixels/s.

A secondary electron SEM image of a drop-cast AuNP on GC, as used for AC-SICM analysis, is shown in Figure 4a (see also SI, Figure S1 for the types of crystallites produced). Hexagonal plates, with the (111) surface parallel to the

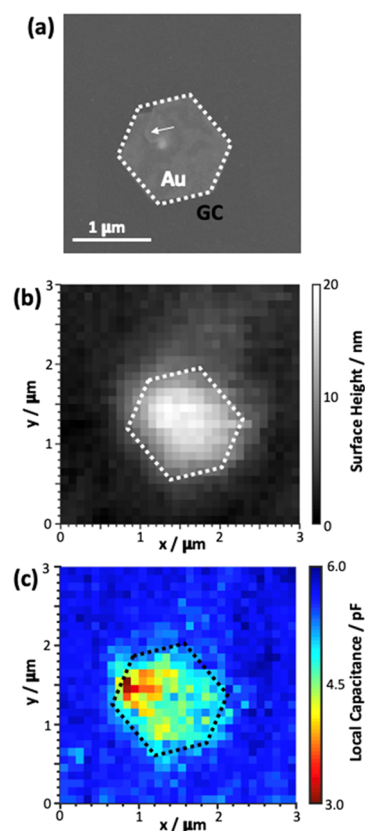


Figure 4. (a) Secondary electron SEM image showing a drop-cast AuNP on GC. The arrow indicates a dislocation in a nanoplate. (b) and (c) show the topography and local capacitance maps of the same area recorded in the AC-SICM configuration at 320 Hz with 50 mV ptp amplitude in 50 mM KCl with a 100 nm radius tip. We scratched the surface of the GC near the AuNP with the nanopipet after the AC-SICM mapping to facilitate the location of the nanoplate in postmortem SEM characterization. Maps contain 30×30 hops (pixels) with no data interpolation. The dotted hexagon indicates the shape of AuNP from the SEM image placed on AC-SICM maps for a visual reference.

substrate, grow via a screw dislocation,⁷⁰ and the patterning commonly visible on the surface of the AuNPs is due to bending or “buckling”^{53,71,72} of the thin plates. As above, AC-SICM parameters were 320 Hz frequency and 50 mV ptp amplitude. The topographical map reveals that the AuNP has a thickness of 10–20 nm (Figure 4b),^{42,53,71,72} although there is some broadening at the edge, which can be attributed to the nonuniform electric field distribution at the nanopipet tip, discussed above.

A phase angle map was acquired simultaneously with the topography data. We used the equivalent circuit in Figure 1a at fixed $R_b = 200 \Omega$, $C_t = 5.5 \text{ pF}$, and $R_t = 110 \text{ M}\Omega$ previously extracted from impedance measurements at a 12 nm tip-to-substrate distance (Table 1) to convert the phase angle values to local capacitance values (Figure 4c). A capacitance map shows a sharp contrast between the AuNP with ca. 4 pF and GC support with ca. 6 pF. Analogous to topographical mapping, the electric field distribution from the nanopipet leads to a broadening of the spatial resolution, so that there is a gradual change of capacitance at the AuNP edge. Despite the compromise of the spatial resolution (vide supra), there is a contrast in the capacitance value across the AuNP, which could be associated with the region of the screw dislocation. We

compared the averaged local C_s values over GC ($=5.8$ pF) and AuNP ($=4.3$ pF) with the global C_s values obtained on GC ($=40$ $\mu\text{F cm}^{-2}$) and Au ($=20$ $\mu\text{F cm}^{-2}$) macroelectrodes (SI, Figure S6). Normalization of C_s values to match local and global measurements yields in a $15\text{--}22$ μm^2 sampled area corresponding to a circle of $2.2\text{--}2.6$ μm in radius, in reasonable agreement with the numerical simulations of the distribution of the electric field reported above (Figure 3b).

4. CONCLUSIONS

Modulating the AC bias between the QRCE in a nanopipet and a conductive substrate in a simple two-electrode SICM configuration enables probe positioning and topographical imaging, based on the measurement of the magnitude of impedance, simultaneously with the determination of local capacitance from the phase angle. The technique is most powerfully implemented in a self-referencing mode, where the impedance is measured with the tip in the bulk and near the surface at each pixel in an image, allowing the local capacitive response of the substrate to be isolated at a single frequency, thus establishing a quantitative footing for the technique. With this approach, it has been possible to acquire data at a reasonable speed of ca. 8 pixels/s, and there is scope for improving this further in the future.

We have shown that impedance measurements in AC-SICM can be readily understood using a simple equivalent circuit model that we developed for Au and GC macroelectrodes and elucidated through approach measurements at different tip-to-substrate distances. This allowed us to identify a window in which the phase is sensitive to the local capacitance of the substrate and the magnitude is sensitive to the surface topography (between ca. 100 Hz and 1 kHz). Further, the technique is amenable to the detailed FEM analysis that aided the optimization of experimental conditions and minimization of frequency dispersion phenomena that can compromise the spatial resolution. Nonetheless, frequency dispersion means that the spatial resolution of AC-SICM is about an order of magnitude larger than the tip size for the studies herein, but FEM modeling will provide a framework to explore whether this could be improved further, for example, by using techniques such as differential concentration SICM.⁷³ Modeling will also be valuable to explore how electrode reactions can be investigated with AC-SICM, which will be a future aim.

Finally, it is worth commenting on some important differences between the two-electrode AC-SICM method described here and conventional SICM, where the second electrode is usually a QRCE in bulk solution. Conventional SICM has been employed to sense the surface charge of highly resistive (living cells) or nonconductive (glass, polymer film) interfaces,^{48,50,57,74} but does not probe the surface charge itself; rather, it senses the ionic atmosphere around charged interfaces through the ion rectification phenomenon under the induced DC ion flow,^{48,59} typically limiting the electrolyte concentrations to a maximum of tens of millimolar (measurements under physiological conditions are possible but require high precision due to the severe compression of the double layer).^{50,75} In contrast, AC-SICM directly probes the electrical properties of the EDL under AC bias of the metal/solution interface. One interesting avenue for future work will be to explore whether this is beneficial in terms of the range of electrolyte conditions that can be studied.

■ ASSOCIATED CONTENT

Supporting Information

The Supporting Information is available free of charge at <https://pubs.acs.org/doi/10.1021/acs.analchem.0c02358>.

SEM image of AuNP drop-casted on GC (SI-1), displacement of z-piezo during approach (SI-2), estimation of thermal drift (SI-3), TEM images of the tip end (SI-4), EIS data in Nyquist coordinates (SI-5), capacitance–potential plots of Au and GC macroelectrodes (SI-6), and FEM model details (SI-7) (PDF)

■ AUTHOR INFORMATION

Corresponding Authors

Viacheslav Shkirskiy – Department of Chemistry, University of Warwick, Coventry CV4 7AL, United Kingdom; orcid.org/0000-0003-4289-9678; Email: slava.shkirskiy@gmail.com

Patrick R. Unwin – Department of Chemistry, University of Warwick, Coventry CV4 7AL, United Kingdom; orcid.org/0000-0003-3106-2178; Email: p.r.unwin@warwick.ac.uk

Authors

Minkyung Kang – Department of Chemistry, University of Warwick, Coventry CV4 7AL, United Kingdom; orcid.org/0000-0003-3248-8496

Ian J. McPherson – Department of Chemistry, University of Warwick, Coventry CV4 7AL, United Kingdom

Cameron L. Bentley – Department of Chemistry, University of Warwick, Coventry CV4 7AL, United Kingdom; orcid.org/0000-0001-7867-6068

Oluwasegun J. Wahab – Department of Chemistry, University of Warwick, Coventry CV4 7AL, United Kingdom

Enrico Daviddi – Department of Chemistry, University of Warwick, Coventry CV4 7AL, United Kingdom; orcid.org/0000-0002-6335-2623

Alex W. Colburn – Department of Chemistry, University of Warwick, Coventry CV4 7AL, United Kingdom

Complete contact information is available at: <https://pubs.acs.org/doi/10.1021/acs.analchem.0c02358>

Notes

The authors declare no competing financial interest.

■ ACKNOWLEDGMENTS

V.S. acknowledges financial support from the European Union's Horizon 2020 research and innovation programme under grant agreement 792948 (NELMA). M.K. acknowledges support from the Leverhulme Trust for an Early Career Fellowship. I.J.M. acknowledges an EPSRC Programme Grant (grant EP/R018820/1), which funds the Crystallisation in the Real World consortium. C.L.B. acknowledges financial support from the Ramsay Memorial Fellowship Trust. O.J.W. acknowledges support from the University of Warwick Chancellor's International Scholarship. P.R.U. thanks the Royal Society for a Wolfson Research Merit Award. This work has been further supported by the EPSRC Faraday Challenge Battery Characterisation (FIRG013).

■ ADDITIONAL NOTE

^aCalculated as $X_C = 1/2\pi fCS$, where X_C is the impedance, f is the frequency, C is the capacitance, and S is the surface area.

REFERENCES

- (1) Chang, B.-Y.; Park, S.-M. *Annu. Rev. Anal. Chem.* **2010**, *3*, 207–229.
- (2) Amirudin, A.; Thierry, D. *Prog. Org. Coat.* **1995**, *26*, 1–28.
- (3) Stratmann, M.; Frankel, G. S. *Corrosion and Oxide Films*. In *Encyclopedia of Electrochemistry*; Bard, A. J.; Stratmann, M., Eds.; Wiley-VCH, 2001.
- (4) Chakri, S.; Patel, A. N.; Frateur, I.; Kanoufi, F.; Sutter, E. M. M.; Tran, T. T. M.; Tribollet, B.; Vivier, V. *Anal. Chem.* **2017**, *89*, 5303–5310.
- (5) Seaman, A.; Dao, T. S.; McPhee, J. J. *Power Sources* **2014**, *256*, 410–423.
- (6) Von Hauff, E. J. *Phys. Chem. C* **2019**, *123*, 11329–11346.
- (7) Isaac, H. S.; Kendig, M. W. *Corrosion* **1980**, *36*, 269–274.
- (8) Lohrengel, M. M.; Heiroth, S.; Kluger, K.; Pilaski, M.; Walther, B. *Electrochim. Acta* **2006**, *51*, 1431–1436.
- (9) Pilaski, M.; Hamelmann, T.; Moehring, A.; Lohrengel, M. M. *Electrochim. Acta* **2002**, *47*, 2127–2134.
- (10) Lohrengel, M. M.; Moehring, A.; Pilaski, M. *Electrochim. Acta* **2001**, *47*, 137–141.
- (11) Hassel, A. W.; Mardare, A. I. J. *Electroanal. Chem.* **2015**, *737*, 93–99.
- (12) Horrocks, B. R.; Schmidtke, D.; Heller, A.; Bard, A. J. *Anal. Chem.* **1993**, *65*, 3605–3614.
- (13) Keddah, M.; Sánchez-Sánchez, C. M.; Vivier, V. Scanning Electrochemical Microscopy in the AC-Mode. In *Encyclopedia of Interfacial Chemistry, Surface Science and Electrochemistry*; Elsevier, 2018; pp 453–464.
- (14) Lucas, M.; Boily, J. F. *Langmuir* **2015**, *31*, 13618–13624.
- (15) Bandarenka, A. S.; Eckhard, K.; Maljusch, A.; Schuhmann, W. *Anal. Chem.* **2013**, *85*, 2443–2448.
- (16) Eckhard, K.; Schuhmann, W. *Analyst* **2008**, *133*, 1486–1497.
- (17) Darowicki, K.; Zieliński, A.; Kurzydłowski, K. J. *Sci. Technol. Adv. Mater.* **2008**, *9*, No. 045006.
- (18) Kalinin, S. V.; Suchomel, M. R.; Davies, P. K.; Bonnell, D. A. J. *Am. Ceram. Soc.* **2002**, *85*, 3011–3017.
- (19) O'Hayre, R.; Lee, M.; Prinz, F. B. *J. Appl. Phys.* **2004**, *95*, 8382–8392.
- (20) Wang, X.; Habte, B. T.; Zhang, S.; Yang, H.; Zhao, J.; Jiang, F.; He, Q. *Anal. Chem.* **2019**, *91*, 11678–11686.
- (21) Arutunow, A.; Darowicki, K.; Tobiszewski, M. T. *Corros. Sci.* **2013**, *71*, 37–42.
- (22) O'Hayre, R.; Feng, G.; Nix, W. D.; Prinz, F. B. *J. Appl. Phys.* **2004**, *96*, 3540–3549.
- (23) Gharbi, O.; Ngo, K.; Turmine, M.; Vivier, V. *Curr. Opin. Electrochem.* **2020**, *20*, 1–7.
- (24) Lillard, R. S.; Moran, P. J.; Isaacs, H. S. *J. Electrochem. Soc.* **1992**, *139*, 1007–1012.
- (25) Huang, V. M.; Wu, S.-L.; Orazem, M. E.; Pébère, N.; Tribollet, B.; Vivier, V. *Electrochim. Acta* **2011**, *56*, 8048–8057.
- (26) Blanc, C.; Orazem, M. E.; Pébère, N.; Tribollet, B.; Vivier, V.; Wu, S. *Electrochim. Acta* **2010**, *55*, 6313–6321.
- (27) Wu, S.; Orazem, M. E.; Tribollet, B.; Vivier, V. *J. Electrochem. Soc.* **2009**, *156*, C28–C38.
- (28) Frateur, I.; Huang, V. M.-W.; Orazem, M. E.; Tribollet, B.; Vivier, V. *Electrochim. Acta* **2008**, *53*, 7386–7395.
- (29) Wu, S.; Orazem, M. E.; Tribollet, B.; Vivier, V. *J. Electrochem. Soc.* **2009**, *156*, C214–C221.
- (30) Mouanga, M.; Puiggali, M.; Tribollet, B.; Vivier, V.; Pébère, N.; Devos, O. *Electrochim. Acta* **2013**, *88*, 6–14.
- (31) Frateur, I.; Huang, V. M.-W.; Orazem, M. E.; Tribollet, B.; Vivier, V. *J. Electrochem. Soc.* **2007**, *154*, C719–C727.
- (32) de Abreu, C. P.; de Assis, C. M.; Suegama, P. H.; Costa, I.; Keddah, M.; de Melo, H. G.; Vivier, V. *Electrochim. Acta* **2017**, *233*, 256–261.
- (33) Ferrari, J. V.; De Melo, H. G.; Keddah, M.; Orazem, M. E.; Pébère, N.; Tribollet, B.; Vivier, V. *Electrochim. Acta* **2012**, *60*, 244–252.
- (34) Galicia, G.; Pébère, N.; Tribollet, B.; Vivier, V. *Corros. Sci.* **2009**, *51*, 1789–1794.
- (35) Annergren, I.; Zou, F.; Thierry, D. *Electrochim. Acta* **1999**, *44*, 4383–4393.
- (36) Shkirskiy, V.; Volovitch, P.; Vivier, V. *Electrochim. Acta* **2017**, *235*, 442–452.
- (37) Shkirskiy, V.; Krasnova, A.; Sanchez, T.; Amar, A.; Vivier, V.; Volovitch, P. *Electrochem. Commun.* **2020**, *111*, No. 106633.
- (38) Wittmann, M. W.; Leggat, R. B.; Taylor, S. R. *J. Electrochem. Soc.* **1999**, *146*, 4071–4075.
- (39) Zou, F.; Thierry, D. *Electrochim. Acta* **1997**, *42*, 3293–3301.
- (40) Jorcin, J. B.; Aragon, E.; Merlatti, C.; Pébère, N. *Corros. Sci.* **2006**, *48*, 1779–1790.
- (41) Zou, F. J. *Electrochem. Soc.* **1997**, *144*, 1957–1965.
- (42) Bentley, C. L.; Unwin, P. R. *Faraday Discuss.* **2018**, *210*, 365–379.
- (43) Momotenko, D.; Byers, J. C.; McKelvey, K.; Kang, M.; Unwin, P. R. *ACS Nano* **2015**, *9*, 8942–8952.
- (44) Momotenko, D.; McKelvey, K.; Kang, M.; Meloni, G. N.; Unwin, P. R. *Anal. Chem.* **2016**, *88*, 2838–2846.
- (45) Ying, L.; Bruckbauer, A.; Zhou, D.; Gorelik, J.; Shevchuk, A.; Lab, M.; Korchev, Y.; Klenerman, D. *Phys. Chem. Chem. Phys.* **2005**, *7*, 2859–2866.
- (46) Chen, C.-C.; Zhou, Y.; Baker, L. A. *Annu. Rev. Anal. Chem.* **2012**, *5*, 207–228.
- (47) Hansma, P. K.; Drake, B.; Marti, O.; Gould, A. C.; Prater, C. B. *Science* **1989**, *243*, 641–643.
- (48) Page, A.; Perry, D.; Unwin, P. R. *Proc. R. Soc. A* **2017**, *473*, 1–34.
- (49) McKelvey, K.; Perry, D.; Byers, J. C.; Colburn, A. W.; Unwin, P. R. *Anal. Chem.* **2014**, *86*, 3639–3646.
- (50) Perry, D.; Paulose Nadappuram, B.; Momotenko, D.; Voyias, P. D.; Page, A.; Tripathi, G.; Frenguelli, B. G.; Unwin, P. R. *J. Am. Chem. Soc.* **2016**, *138*, 3152–3160.
- (51) Perry, D.; Al Botros, R.; Momotenko, D.; Kinnear, S. L.; Unwin, P. R. *ACS Nano* **2015**, *9*, 7266–7276.
- (52) Kang, M.; Momotenko, D.; Page, A.; Perry, D.; Unwin, P. R. *Langmuir* **2016**, *32*, 7993–8008.
- (53) Shankar, S. S.; Rai, A.; Ankamwar, B.; Singh, A.; Ahmad, A.; Sastry, M. *Nat. Mater.* **2004**, *3*, 482–488.
- (54) Bentley, C. L.; Perry, D.; Unwin, P. R. *Anal. Chem.* **2018**, *90*, 7700–7707.
- (55) McKelvey, K.; Perry, D.; Byers, J. C.; Colburn, A. W.; Unwin, P. R. *Anal. Chem.* **2014**, *86*, 3639–3646.
- (56) Perry, D.; Momotenko, D.; Lazenby, R. A.; Kang, M.; Unwin, P. R. *Anal. Chem.* **2016**, *88*, 5523–5530.
- (57) Perry, D.; Momotenko, D.; McKelvey, K.; Unwin, P. R.; Kinnear, S. L. *J. Am. Chem. Soc.* **2014**, *136*, 13735–13744.
- (58) Nesbitt, H. W. *Chem. Geol.* **1984**, *43*, 127–142.
- (59) Sa, N.; Lan, W. J.; Shi, W.; Baker, L. A. *ACS Nano* **2013**, *7*, 11272–11282.
- (60) Kang, M.; Perry, D.; Bentley, C. L.; West, G.; Page, A.; Unwin, P. R. *ACS Nano* **2017**, *11*, 9525–9535.
- (61) Momotenko, D.; Cortés-Salazar, F.; Josserand, J.; Liu, S.; Shao, Y.; Girault, H. H. *Phys. Chem. Chem. Phys.* **2011**, *13*, 5430–5440.
- (62) White, H. S.; Bund, A. *Langmuir* **2008**, *24*, 2212–2218.
- (63) Nadappuram, B. P.; McKelvey, K.; Botros, R. A.; Colburn, A. W.; Unwin, P. R. *Anal. Chem.* **2013**, *85*, 8070–8074.
- (64) Edmondson, J. F.; Meloni, G. N.; Costantini, G.; Unwin, P. R. *ChemElectroChem* **2020**, *7*, 697–706.
- (65) Feng, J.; Liu, J.; Wu, B.; Wang, G. *Anal. Chem.* **2010**, *82*, 4520–4528.
- (66) Newman, J.; Thomas-Alyea, K. *Electrochemical Systems*, 3rd ed.; Wiley, 2004.
- (67) Wang, Y.; Shan, X.; Wang, S.; Tao, N.; Blanchard, P. Y.; Hu, K.; Mirkin, M. V. *Anal. Chem.* **2016**, *88*, 1547–1552.
- (68) Newman, J. J. *Electrochem. Soc.* **1970**, *117*, 198–203.
- (69) Gharbi, O.; Dizon, A.; Orazem, M. E.; Tran, M. T. T.; Tribollet, B.; Vivier, V. *Electrochim. Acta* **2019**, *320*, No. 134609.

- (70) Zhai, Y.; Zhang, F.; Zhang, B.; Gao, X. *Adv. Mater.* **2017**, *29*, No. 1703102.
- (71) Grzelczak, M.; Pérez-Juste, J.; Mulvaney, P.; Liz-Marzán, L. M. *Chem. Soc. Rev.* **2008**, *37*, 1783–1791.
- (72) Shao, Y.; Jin, Y.; Dong, S. *Chem. Commun.* **2004**, *10*, 1104–1105.
- (73) Perry, D.; Page, A.; Chen, B.; Frenguelli, B. G.; Unwin, P. R. *Anal. Chem.* **2017**, *89*, 12458–12465.
- (74) Page, A.; Perry, D.; Young, P.; Mitchell, D.; Frenguelli, B. G.; Unwin, P. R. *Anal. Chem.* **2016**, *88*, 10854–10859.
- (75) Bentley, C. L.; Edmondson, J.; Meloni, G. N.; Perry, D.; Shkirskiy, V.; Unwin, P. R. *Anal. Chem.* **2019**, *91*, 84–108.